Accepted Manuscript

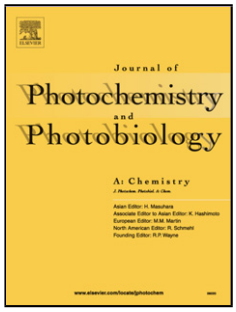

Title: Improvement of sol-gel prepared tungsten trioxide photoanodes upon doping with ytterbium

Authors: Ana Korina Díaz-García, Roberto Gómez

PII: S1010-6030(17)31695-7
DOI: https://doi.org/10.1016/j.jphotochem.2018.03.008
Reference: JPC 11177

To appear in: *Journal of Photochemistry and Photobiology A: Chemistry*

Received date: 15-11-2017
Revised date: 19-1-2018
Accepted date: 5-3-2018

Please cite this article as: Ana Korina Díaz-García, Roberto Gómez, Improvement of sol-gel prepared tungsten trioxide photoanodes upon doping with ytterbium, Journal of Photochemistry and Photobiology A: Chemistry https://doi.org/10.1016/j.jphotochem.2018.03.008

Improvement of sol-gel prepared tungsten trioxide photoanodes upon doping with ytterbium

Ana Korina Díaz-García and Roberto Gómez*

Departament de Química Física i Institut Universitari d'Electroquímica, Universitat d'Alacant, Apartat 99, E-03080 Alacant, Spain

*corresponding author: e-mail: roberto.gomez@ua.es; phone: +34 965903748

HIGHLIGHTS

- A sol-gel method for the preparation of Yb-doped WO_3 photoanodes is presented.
- Ytterbium modification induces an increase in the photoresponse of WO_3 electrodes.
- Yb changes WO_3 morphology and surface charge without increasing carrier density.

Abstract

The development of efficient and stable photoelectrodes keeps on being critical in the development of practical water splitting devices. Sol-gel synthesized tungsten trioxide thin film electrodes modified with ytterbium have been prepared on conducting glass substrates. All the obtained electrodes were found to be composed of monoclinic WO_3,

which is the photoactive crystal phase of WO_3 for water oxidation. The photoelectrochemical behavior of both WO_3 and WO_3:Yb nanostructured electrodes in 0.1 M $HClO_4$ is apparently characterized by a low degree of recombination. Ytterbium addition to tungsten trioxide improves its photoelectrochemical response as larger photocurrents are obtained without a significant change of the onset potential. This behavior is attributed primarily to a surface effect rather than on bulk doping. The addition of H_2O_2 to the aqueous electrolyte gives rise to both an increment in photocurrent and a shift of the photocurrent onset potential toward less positive values, which can be linked to the fact that hydrogen peroxide acts as an efficient hole scavenger. The implications of these findings in the mechanism of water photooxidation on WO_3 are discussed.

Keywords: photoelectrochemical, tungsten trioxide, water splitting, ytterbium doping.

1. Introduction

Nowadays, the depletion of fossil energy resources is a serious problem which will be affecting modern life as we conceive it now. Finding carbon free energy sources is one of the most pressing challenges of humanity [1,2]. Furthermore, since Fujishima and Honda published the first photoelectrochemical (PEC) water splitting study in 1972 [3], hydrogen has been widely studied as a promising energy vector that can be produced in a renewable way. Taking into account that solar energy is an inexhaustible natural resource and that hydrogen is a potential candidate to be used as a clean fuel, solar water splitting seems to be one of the most convenient ways to harvest solar light and to convert it into chemical energy, hydrogen for instance [4-6].

Most of the PEC devices work in combination with photovoltaic elements (e.g., p-n junctions) and contain one photoelectrode (normally a photoanode) and one dark electrode [6]. Nevertheless, a more straightforward and potentially more efficient path to light-driven chemical transformations is to directly interface semiconductors and an appropriate electrolyte in a PEC tandem cell, where there is one photoanode and one photocathode [7-9]. If we focus on oxide electrodes, Sivula et al. [9] have shown that a bismuth vanadate-cuprous oxide tandem cell for overall solar water splitting can work without applying an external potential, although the stability of the oxide electrodes is limited.

Photoanodes used in PEC water splitting are n-type semiconductors that under illumination can photogenerate holes that oxidize water into O_2. They mainly include various binary and ternary oxides [5], for instance, α-Fe_2O_3 [10,11], WO_3 [12-15], ZnO [16,17], In_2O_3 [18], SnO_2 [19], TiO_2 [20-21], $BiVO_4$ [22-24], $CuWO_4$ [24,25], Bi_2WO_6 [25], and bismuth molybdates ($Bi_2O_3{\cdot}nMoO_3$) [26]. Among them, tungsten oxide (WO_3) has been extensively studied as a photoanode for use in solar water splitting since its valence band maximum position can provide sufficient overpotential for

photogenerated holes to oxidize water [27]. Furthermore, WO_3 is not only inexpensive and nontoxic, but also it is one of the few oxides that are stable in acidic aqueous media, which opens up the possibility of preparing tandem cells based on acidic electrolytes [5,13,28].

The photooxidation of small organic molecules in competition with that of water has been studied as a way to understand the photoelectrochemical response of WO_3 photoanodes and to assess their potential use in decontaminative photoelectrocatalysis [29,30]. It is remarkable that in all cases a very high conversion efficiency value was found. The oxidation of formic acid not only on electrodeposited, but also on doctor-blade deposited WO_3 nanostructured thin film electrodes has been studied [13], being reported in both cases photocurrent doubling and a shift of the photocurrent onset potential toward less positive values. Remarkably, adding small organic molecules improves photoelectrochemical behavior as these species tend to be more easily oxidized than water molecules [13,31].

Other convenient ways for enhancing the photoelectrochemical performance of WO_3 are modifying both morphology and/or composition (doping) [4,27]. Kalanur et al. [32], demonstrated that a significant increase in photocurrent is linked to the existence of direct pathways for electron transport such as those provided by vertically aligned nanorod arrays of WO_3. Regarding doping, WO_3 has been doped with elements such as nitrogen [33,34], carbon [35], tellurium [36], cesium [37], and ytterbium [38]. Liew et al. [38] prepared Yb-doped WO_3 by co-sputtering and found an improvement in photocurrent density, which was attributed to conductive carrier path and increased oxygen vacancies due to the substitution of $W^{6+}$by $Yb^{3+}$and electron enrichment by the $4f^{13}$ orbital configuration of Yb^{3+}. Furthermore, they showed that Yb incorporation reduced charge transfer resistances and increased donor densities of WO_3 photocatalysts. It is also worth noting that recent work in our laboratory has shown that Yb doping of hematite electrodes is effective for promoting photoactivity [39].

In this work, we report on the behavior of WO_3 thin film electrodes prepared by a novel sol-gel procedure with a focus on their structural, morphological and photoelectrochemical properties. In addition, WO_3 thin film electrodes were modified with ytterbium for the first time following a sol-gel procedure. It should be highlighted that our work is focused in ultrathin films since this avoids difficulties arising from composition variations throughout the thickness of the electrode as well as complexities derived from inhomogeneous illumination. This facilitates gaining physical insight on the dopant effect. In order to find the optimum amount of dopant for an enhanced photoelectrochemical behavior, WO_3 electrodes were doped with five different atomic percentages of ytterbium. The photoelectrochemical response of, not only WO_3 electrodes, but also WO_3:Yb in contact with a more effective hole scavenger than water has also been addressed. Important features of those electrodes such as photocurrent onset potential, photoactivity improvement and chemical stability are highlighted.

2. Experimental

WO_3 photoanodes were prepared on commercial fluorine-doped tin oxide (FTO) glass substrates by spin-coating followed by a two-step thermal treatment. WCl_6 (150 mg, purity 99.99%+, Aldrich Chem. Co.) and polyethylene glycol (25 mg, purity 99%, Aldrich Chem. Co.) were dissolved in 1.25 mL ethanol and stirred for 4 hours [40]. Then, this precursor was spin-coated onto FTO at 1500 rpm for 15 s. The samples were dried, maintained at 40 ºC in air for 30 minutes and then, annealed at 500 ºC for 30 minutes at a ramp rate of 5 ºC/min. On the other hand, to obtain WO_3 doped with Yb (0.1, 0.2, 0.3, 0.4 y 0.5 %at Yb), $YbCl_3 \cdot 6H_2O$ (purity 99.99%+, Aldrich Chem. Co.) was added to the precursor solution at the beginning of the synthetic procedure.

A Bruker D8-Advance X-ray diffractometer operating with Cu-K radiation at 40 kV and 40 mA was used to obtain the X-ray diffraction patterns. The composition of the electrodes was analyzed by X-ray photoelectron spectroscopy (XPS) using a Kα Thermoscientific spectrometer. The electrode morphology was studied with a Zeiss model MERLIN compact VP field emission scanning electron microscope (FE-SEM). The optical characterization of the electrodes was performed by solid-state UV-vis spectroscopy, using a Shimadzu UV-2401 PC spectrophotometer equipped with an integrating sphere. The UV-vis spectral data for the annealed films coated on transparent FTO conducting substrates were recorded in the absorbance mode.

Photoelectrochemical measurements were performed at room temperature using a three-electrode cell provided with a fused silica window and a computer-controlled Autolab PGSTAT30 potentiostat. In all cases, an Ag/AgCl/KCl(sat) electrode and a Pt wire were employed as a reference and counter electrode, respectively. All the potentials are referred to the Ag/AgCl/KCl(sat) electrode. Solutions of 0.1 M $HClO_4$ were used as working electrolytes. They were prepared with ultrapure water and N_2-purged before the experiments. The illumination was carried from the electrolyte side (EE illumination) by employing a 300 W Xe-arc lamp (Thermo Oriel) equipped with a water filter. The light intensity was 0.120 $mW \cdot cm^{-2}$ and it was measured by coupling an optical power meter (Thorlabs model PM100D) with a thermopile.

3. Results and discussions

3.1. Structural and physical characterization.

To verify the chemical structure of the as-prepared thin films, they were analyzed by XRD. For WO_3 and WO_3:Yb 0.2 at% samples, their XRD patterns shown in Fig. 1

indicate that the WO_3 monoclinic phase (JCPDS 01-072-0677) is the only crystalline phase detected for both samples, which is the polymorph of WO_3 more photoactive for water oxidation [32]. Therefore the introduction of small quantities of the dopant does not trigger any structural transformation.

Fig. 2 illustrates the morphology of the WO_3 thin films with and without Yb. In both cases, nanocrystals are homogeneously distributed on the surface, being connected to one another. Grains have an average diameter close to 60 nm not only for both samples although it appears to be slightly smaller in the case of the WO_3:Yb sample (see histograms in the insets). Particle arrangement seems to be more uniform for WO_3:Yb, which can be attributed to a change of the sol-gel process included by the presence of Yb. In addition, the size distribution is more symmetrical and slightly narrower for Yb-doped samples.

In order to confirm that Yb is effectively introduced in the WO_3 matrix, XPS analysis was performed, being the high resolution spectra for the W 4f, O 1s and Yb 4d regions displayed in Figure 3. The results point to the presence of Yb in the WO_3:Yb sample, which means that the incorporation of Yb is successfully performed. As expected for the small loading of Yb in the sample doped and intrinsic WO_3 films show a similar W 4f spectra, which consists of two peaks centered at 35.46 eV and 37.58 eV associated with the spin-orbit doublet of W $4f_{7/2}$ and W $4f_{5/2}$ respectively. The O 1s spectra are also similar for both samples showing a peak at 530.28 eV typical of O-W bonding and a shoulder at 531.87 eV typical of O-C bonding coming from spurious impurities [38]. For the Yb 4d spectrum, a broad peak of low intensity at 185.1 eV can be assigned to Yb $4d_{5/2}$ in good agreement with reported value of 185.0 eV for Yb_2O_3 by Uwamino et al. [41]. This means that the environment for Yb in the WO_3 lattice is similar to that found in Yb_2O_3 (+3 oxidation state and coordination to oxygen). It is worth noting that even when 0.2 at% doped samples were prepared, a composition of 0.24 at% was reported

by XPS analysis, which suggests that there is a slight enrichment of Yb on the thin film surface.

The optical bandgap was obtained from optical absorption experiments. Fig. 4a shows the optical absorption spectra of WO_3 and WO_3:Yb 0.2 at% samples, which are very similar. However, WO_3:Yb samples have a slightly higher absorption background and there is a minor shift in the absorption edge. Figure 4b shows the Tauc plot of $(Ahv)^{1/2}$ versus *hv* (*A* is the absorbance and *hv* the incident photon energy). Extrapolating the linear region, the value of E_g is estimated to be 2.65 eV for both pristine and doped WO_3 samples, in agreement with the values between 2.6 and 2.8 eV reported in the literature [2,5].

3.2. Electrochemical characterization.

Cyclic voltammograms (CV) for WO_3 and WO_3:Yb 0.2 at% electrodes in the dark are shown in Fig. 5 in 0.1 M both in the dark (a) and under illumination (b). In the dark, the electrochemical response exhibits the existence of small capacitive currents in the low potential region (below 0.2 V), which tend to be higher when ytterbium is present. As these currents have demonstrated to be proportional to the interfacial area [21], it seems that the Yb-induced change could be mainly due to small changes in particle size and distribution as observed in Fig. 2. Importantly, the addition of Yb to the WO_3 structure does not alter the shape of the voltammograms in the accumulation region, which point to the fact that doping does not alter in a significant way the conduction band/band gap states. In addition, this quasi-reversible process appears accompanied by blue coloration of the film at negative potentials. This process can be explained on the basis of proton intercalation leading to a colored tungsten bronze [Eq. (1)]:

$$xH^+ + xe^- + WO_3 \Leftrightarrow H_xWO_3 \qquad (1)$$

Linear scan voltammograms performed under chopped illumination for WO_3 and WO_3:Yb at. 0.2 at% electrodes are shown in Fig. 5 (b). Upon illumination, anodic photocurrents appear with an onset potential at 0.30 $V_{Ag/AgCl}$, that is, at 0.55 V versus the reversible hydrogen electrode (RHE). In agreement with previous reports [13,42], the material behaves as an n-type semiconductor with a valence band located at around 3.2 V_{RHE} (by considering a bandgap value of 2.65 eV as determined above). Furthermore, there is an increase in the photocurrent density for WO_3:Yb 0.2 at% samples.

The n-type behavior of the as-prepared electrodes was confirmed by constructing Mott-Schottky plots (Fig. 6, Fig. S1) at two different frequencies in the dark and under illumination in 0.1 M $HClO_4$. The slopes of the linear regions increase with frequency and for each frequency, the slope decreases in the order WO_3 < WO_3:Yb. This behavior in the slope might be directly related with a change not only in donor density but also in roughness of the electrode material, as it has been proposed by Gómez and coworkers [11]. In other words, since the real interfacial area for WO_3 electrodes is much larger than the geometric one and, as long as characteristic dimension of the nano-objects is larger than that of the space charge region, the Mott-Schottky equation should be written as [Eq. (2)]:

$$\frac{A_{real}^2}{C_{SC}^2} = \frac{2}{e\varepsilon_{sc}\varepsilon_0 N_d}\left(E - E_{fb} - \frac{kT}{e}\right) \quad (2)$$

where C_{sc} is the capacitance of the space charge region, A_{real} is the real surface area, which takes into account the electrode roughness, $\mathcal{E}_{sc}$ is the semiconductor dielectric constant, $\mathcal{E}_0$ is the vacuum permittivity, N_d is the donor density, E is the applied potential, and E_{fb} is the flat band potential. Taking into account that the roughness factor (r) can be expressed as [Eq. (3)]:

$$r = \frac{A_{real}}{A_{geom}} \quad (3)$$

where A_{geom} is the geometric (projected) area of the electrode, Equation 2 can be rewritten as [Eq. (4)]:

$$\frac{A_{geom}^2}{C_{SC}^2} = \frac{2}{e\varepsilon_{sc}\varepsilon_0 N_d r^2}\left(E - E_{fb} - \frac{kT}{e}\right) \quad (4)$$

To analyze the difference in the slopes, we must take into account that:

- The SEM analysis suggests that roughness factor is higher for WO_3:Yb than for WO_3, as the average particle size is slightly smaller for the Yb-containing sample.
- The capacity of the accumulation region for WO_3:Yb is higher than for WO_3 (Fig. 5a), which is related with the real area of the electrodes, which means that roughness is higher for WO_3:Yb than for WO_3.

Therefore, if $r_{WO3:Yb} > r_{WO3}$, it must occur that $N_{d,WO3:Yb} < N_{d,WO3}$. This behavior might be related to a diminution of the density of oxygen vacancies upon addition of Yb [43]. The diminution in donor density is concomitant with an enhancement of the n-type behavior of the electrode. Such an apparent contradiction can be understood on the bases of an increase in electron mobility upon Yb doping even when their concentration decreases.

The flat band potential estimated from extrapolation of the intercept of the Mott-Schottky plot linear region with the *x*-axis, has approximately the same value (-0.05 $V_{Ag/AgCl}$) for pure WO_3 and WO_3:Yb electrodes. It is worth noting that this value is close to that of the photocurrent onset, indicating that surface recombination is limited in both cases. In agreement, the flat band potential does not significantly shift upon illumination, which means that the density of trapped holes under photostationary conditions when the illumination is intense does not induce an upward shift of the flat band potential.

The dependence of the photocurrent density on the atomic percent of Yb in the WO_3 electrodes is shown in Fig. 7 for two different values of the applied potential. Five

different amounts of atomic percentages (0.1, 0.2, 0.3, 0.4 and 0.5 at. %) were studied as to optimize the doping condition. As observed, the photocurrent is higher for the 0.2 at% sample not only at 0.6 V but also at 1.2 V. Thus, this is the adequate level of doping for a higher photoresponse. It should be emphasized that the observed non-linear dependence of the photoactivity on dopant concentration probably reflects the concurrence of several factors in determining the effect of Yb doping.

Fig. 8 shows the voltammetric behavior both in the dark and under illumination for pristine and Yb-modified WO_3 in the presence 0.1 M H_2O_2. The dark response of the WO_3 electrodes is characterized by the development of large cathodic currents associated to the reduction of H_2O_2 whose onset coincides with that of the accumulation region. Upon illumination and irrespective of the presence of Yb, there is a shift of the onset potential toward less positive values and an increase in the photocurrent as observed by Gómez and coworkers [13] in the case of formic acid photooxidation. This is a consequence of adding H_2O_2, which can be linked to the fact that the hydrogen peroxide acts as an efficient hole scavenger. However, the increment in the photocurrent density of WO_3:Yb at. 0.2% atomic samples keeps on occurring at a level similar to that in the absence of H_2O_2. One should conclude that the improvement caused by doping with Yb is not directly linked to the charge transfer process, indirectly supporting the increase in electron mobility invoked above.

The efficiency of H_2O_2 as a hole scavenger is quite evident. Water photooxidation could follow two possible pathways depicted in [Eq.(5)] and [Eq.(6)]:

$$2H_2O + 4h^+ \rightarrow O_2 + 4H^+,\ E^\circ = 1.229\ V\ (vs.\ NHE) \qquad (5)$$

$$2H_2O + 2h^+ \rightarrow H_2O_2 + 2H^+,\ E^\circ = 1.763\ V\ (vs.\ NHE) \qquad (6)$$

In this context, [Eq.(5)], which does not consider direct formation of H_2O_2, is thermodynamically favorable, since the standard potential is significantly smaller than when its formation is required [Eq.(6)]. However, in a case when H_2O_2 is already

present in the solution, its conversion to oxygen [Eq.(7)] becomes the primary reaction as the standard potential for this process is much lower than for the competitive process of water photooxidation according to the [Eq.(5)]. The latter illustrates the fact that H_2O_2 can be readily oxidized even in the absence of a strong oxidizing agents (e.g. holes), and thus serve as a very efficient hole scavenger.

$$H_2O_2 \rightarrow O_2 + 2H^+ + 2e^-,\ E^\circ = -0.695\ V\ (vs.\ NHE) \qquad (7)$$

Based on these observations, it is plausible to assume that the formation of peroxo species is limiting the rate of water oxidation on WO_3 photoanodes.

Finally, the pH effect is summarized in Fig. 9, which shows that the higher the pH value, the worst the photoresponse. It is worth noting that in the case of water photooxidation the WO_3:Yb electrode is much more sensitive to pH than the pristine WO_3 electrode. This could be linked with the fact that there is Yb located at the surface, as demonstrated by XPS analysis, and the acid-base properties of the W-O and Yb-O species might be different, as well as, their isoelectric points (IEP), since IEP of Yb_2O_3 is located at pH values around 7.5 – 8.5 while that of WO_3 is located at pH values at around 1.5 – 2 [44]. Therefore, the change in the charge state of the surface (resulting from acid/base equilibria) would be the main factor responsible for the effects observed as a function of pH without the need of invoking Yb surface enrichment.

4. Conclusions

In summary, we have shown that Yb modification of sol-gel synthesized tungsten trioxide improves its photoelectrochemical response as photocurrents increase while the onset potential remains virtually unaltered. Taking into account Mott-Schottky plots, this behavior is attributed to a surface effect and/or to an increase in electron mobility together with a slight diminution in particle size upon Yb modification. In addition, since

doping does not cause a significant alteration of the shape of the dark CVs in the accumulation region, no significant changes in the conduction band/band gap states seem to occur upon doping. Different doping levels were studied and the highest photocurrent was obtained for 0.2 at% Yb. The photoelectrochemical behavior of both WO_3 and WO_3:Yb nanostructured electrodes in aqueous solutions of 0.1 M $HClO_4$ is apparently characterized by a low degree of recombination. As a result, the addition of H_2O_2 to the aqueous electrolyte only gives rise to a moderate increment in photocurrent and a slight shift of the photocurrent onset potential towards less positive values, despite H_2O_2 being a very effective hole scavenger. Importantly, the addition of H_2O_2 causes similar effects regardless the presence of Yb, meaning that factors different from the hole transfer process, such as charge carrier mobility play a crucial role in the Yb-induced enhancement.

5. Acknowledgements

Financial support of the Spanish Ministry of Economy and Competitiveness through the project MAT2015-71727-R (FONDOS FEDER) is gratefully acknowledged. A. K. D.-G. thanks the Mexican government (CONACyT) for the award of a doctoral grant.

References

[1] M.G. Walter, E.L. Warren, J.R. McKone, S.W. Boettcher, Q. Mi, E.A. Santori, N.S. Lewis, Solar water splitting cells, Chem. Rev. 110 (2010) 6446–6473. doi:10.1021/cr1002326.

[2] C. Janáky, K. Rajeshwar, N.R. de Tacconi, W. Chanmanee, M.N. Huda, Tungsten-based oxide semiconductors for solar hydrogen generation, Catal. Today. 199 (2013) 53–64. doi:10.1016/j.cattod.2012.07.020.

[3] A. Fujishima, K. Honda, Electrochemical photolysis of water at a semiconductor electrode., Nature. 238 (1972) 37–38. doi:10.1038/238037a0.

[4] T. Zhu, M.N. Chong, E.S. Chan, Nanostructured Tungsten Trioxide Thin Films Synthesized for Photoelectrocatalytic Water Oxidation: A review, ChemSusChem. 7 (2014) 2974–2997. doi:10.1002/cssc.201402089.

[5] D. Kang, T.W. Kim, S.R. Kubota, A.C. Cardiel, H.G. Cha, K.-S. Choi, Electrochemical Synthesis of Photoelectrodes and Catalysts for Use in Solar Water Splitting, Chem. Rev. 115 (2015) 12839–12887. doi:10.1021/acs.chemrev.5b00498.

[6] K. Sivula, Toward Economically Feasible Direct Solar-to-Fuel Energy Conversion, J. Phys. Chem. Lett. 6 (2015) 975–976. doi:10.1021/acs.jpclett.5b00406.

[7] K. Ohashi, J. McCann, J.O. Bockris, Stable photoelectrochemical cells for the splitting of water, Nature. 266 (1977) 610–611. doi:10.1038/266610a0.

[8] S. Ida, K. Yamada, T. Matsunaga, H. Hagiwara, Y. Matsumoto, T. Ishihara, Preparation of p-type $CaFe_2O_4$ photocathodes for producing hydrogen from water, J. Am. Chem. Soc. 132 (2010) 17343–17345. doi:10.1021/ja106930f.

[9] P. Bornoz, F.F. Abdi, S.D. Tilley, B. Dam, R. Van De Krol, M. Grätzel, K. Sivula, A bismuth vanadate-cuprous oxide tandem cell for overall solar water splitting, J. Phys. Chem. C. 118 (2014) 16959–16966. doi:10.1021/jp500441h.

[10] M. Li, Z. Zhang, F. Lyu, X. He, Z. Liang, M.-S. Balogun, X. Lu, P.-P. Fang, Y. Tong, Facile Hydrothermal Synthesis of Three Dimensional Hematite Nanostructures with Enhanced Water Splitting Performance, Electrochim. Acta. 186 (2015) 95–100. doi:10.1016/j.electacta.2015.10.048.

[11] A. Cots, D. Cibrev, P. Bonete, R. Gómez, Hematite Nanorod Electrodes Modified with Molybdenum: Photoelectrochemical Studies, ChemElectroChem. 4 (2017) 1–10.

doi:10.1002/celc.201600644.

[12] S. Shin, H.S. Han, J.S. Kim, I.J. Park, M.H. Lee, K.S. Hong, I.S. Cho, Tree-like Nanoporous WO_3 Photoanode with Enhanced Charge Transport Efficiency for Photoelectrochemical Water Oxidation, J. Mater. Chem. A. 3 (2015) 12920–12926. doi:10.1039/C5TA00823A.

[13] D. Monllor-Satoca, L. Borja, A. Rodes, R. Gómez, P. Salvador, Photoelectrochemical behavior of nanostructured WO_3 thin-film electrodes: The oxidation of formic acid, ChemPhysChem. 7 (2006) 2540–2551. doi:10.1002/cphc.200600379.

[14] S. Sfaelou, L.-C. Pop, O. Monfort, V. Dracopoulos, P. Lianos, Mesoporous WO_3 photoanodes for hydrogen production by water splitting and PhotoFuelCell operation. International Journal of Hydrogen Energy 41 (2016) 5902-5907. doi:10.1016/j.ijhydene.2016.02.063.

[15] D. Raptis, V. Dracopoulos, P. Lianos, Renewable energy production by photoelectrochemical oxidation of organic wastes using WO_3 photoanodes, Journal of Hazardous Materials 333 (2017) 259-264. doi:10.1016/j.jhazmat.2017.03.044.

[16] A.K. Chandiran, M. Abdi-Jalebi, M.K. Nazeeruddin, M. Grätzel, Analysis of Electron Transfer Properties of ZnO and TiO_2 Photoanodes for Dye-Sensitized Solar Cells, ACS Nano. 8 (2014) 2261–2268. doi:10.1021/nn405535j.

[17] P. Pratim, S. Mukhopadhyay, S.A. Agarkar, A. Jana, P.S. Devi, Photochemical performance of ZnO nanostructures in dye sensitized solar cells, Solid State Sci. 48 (2015) 237–243. doi: 10.1016/j.solidstatesciences.2015.08.014.

[18] E.P. Surovoi, G.O. Ramazanova, Photostimulated growth of In-In_2O_3 films, Inorg. Mater. 49 (2013) 988–992. doi:10.1134/S0020168513090185.

[19] I. Bedja, S. Hotchandani, P. Kamat, Preparation and Photoelectrochemical Characterization of Thin, J. Phys. Chem. 98 (1994) 4133–4140. doi:10.1021/j100066a037.

[20] M. Jankulovska, T. Lana-Villarreal, R. Gómez, Hierarchically organized titanium dioxide nanostructured electrodes: Quantum-sized nanowires grown on nanotubes, Electrochem. Commun. 12 (2010) 1356–1359. doi:10.1016/j.elecom.2010.07.019.

[21] T. Berger, D. Monllor-Satoca, M. Jankulovska, T. Lana-Villarreal, R. Gómez, The electrochemistry of nanostructured titanium dioxide electrodes, ChemPhysChem. 13 (2012) 2824–2875. doi:10.1002/cphc.201200073.

[22] A. Kudo, K. Omori, H. Kato, A novel aqueous process for preparation of crystal form-controlled and highly crystalline $BiVO_4$ powder from layered vanadates at room temperature and its photocatalytic and photophysical properties, J. Am. Chem. Soc. 121 (1999) 11459–11467. doi:10.1021/ja992541y.

[23] J. Quiñonero, T. Lana-Villarreal, R. Gómez, Improving the photoactivity of bismuth vanadate thin film photoanodes through doping and surface modification strategies, Appl. Catal. B Environ. 194 (2016) 141–149. doi:10.1016/j.apcatb.2016.04.057.

[24] J.E. Yourey, B.M. Bartlett, Electrochemical deposition and photoelectrochemistry of $CuWO_4$, a promising photoanode for water oxidation, J. Mater. Chem. 21 (2011) 7651–7660. doi:10.1039/c1jm11259g.

[25] J.C. Hill, K.-S. Choi, Synthesis and characterization of high surface area $CuWO_4$ and Bi_2WO_6 electrodes for use as photoanodes for solar water oxidation, J. Mater. Chem. A. 1 (2013) 5006–5014. doi:10.1039/c3ta10245a.

[26] J. Yu, A. Kudo, Hydrothermal Synthesis and Photocatalytic Property of 2-Dimensional Bismuth Molybdate Nanoplates, Chem. Lett. 34 (2005) 1528–1529. doi:10.1246/cl.2005.1528.

[27] X. Liu, F. Wang, Q. Wang, Nanostructure-based WO_3 photoanodes for photoelectrochemical water splitting, Phys. Chem. Chem. Phys. 14 (2012) 7894–7911. doi:10.1039/c2cp40976c.

[28] A. Tacca, L. Meda, G. Marra, A. Savoini, S. Caramori, V. Cristino, C.A. Bignozzi, V. Gonzalez Pedro, P.P. Boix, S. Gimenez, J. Bisquert, Photoanodes based on nanostructured WO_3 for water splitting., Chemphyschem. 13 (2012) 3025–3034. doi:10.1002/cphc.201200069.

[29] C. Santato, M. Ulmann, J. Augustynski, Photoelectrochemical Properties of Nanostructured Tungsten Trioxide Films, J. Phys. Chem. B. 105 (2001) 936–940. doi:10.1021/jp002232q.

[30] R. Solarska, C. Santato, C. Jorand-Sartoretti, M. Ulmann, J. Augustynski, Photoelectrolytic oxidation of organic species at mesoporous tungsten trioxide film electrodes under visible light illumination, J. Appl. Electrochem. 35 (2005) 715–721. doi:10.1007/s10800-005-1400-x.

[31] R. Reichert, C. Zambrzycki, Z. Jusys, R.J. Behm, Photo-electrochemical Oxidation of Organic C1 Molecules over WO_3 Films in Aqueous Electrolyte: Competition Between Water Oxidation and C1 Oxidation, ChemSusChem. 8 (2015) 3677–3687. doi:10.1002/cssc.201500800.

[32] S.S. Kalanur, Y.J. Hwang, S.Y. Chae, O.S. Joo, Facile growth of aligned WO_3 nanorods on FTO substrate for enhanced photoanodic water oxidation activity, J. Mater. Chem. A. 1 (2013) 3479–3488. doi:10.1039/c3ta01175e.

[33] B. Cole, B. Marsen, E. Miller, Y. Yan, B. To, K. Jones, M. Al-Jassim, Evaluation of Nitrogen Doping of Tungsten Oxide for Photoelectrochemical Water Splitting, J. Phys. Chem. C. 112 (2008) 5213–5220. doi:10.1021/jp077624c.

[34] Y.-C. Nah, I. Paramasivam, R. Hahn, N.K. Shrestha, P. Schmuki, Nitrogen doping of nanoporous WO_3 layers by NH_3 treatment for increased visible light photoresponse, Nanotechnology. 21 (2010) 105704 (5pp). doi:10.1088/0957-4484/21/10/105704.

[35] Y. Sun, C.J. Murphy, K.R. Reyes-Gil, E.A. Reyes-Garcia, J.M. Thornton, N.A. Morris, D. Raftery, Photoelectrochemical and structural characterization of carbon-doped WO_3 films prepared via spray pyrolysis, Int. J. Hydrogen Energy. 34 (2009) 8476–8484. doi:10.1016/j.ijhydene.2009.08.015.

[36] B. Yang, V. Luca, Enhanced long-wavelength transient photoresponsiveness of WO_3 induced by tellurium doping, Chem. Commun. (2008) 4454–4456. doi:10.1039/b807629d.

[37] Y. Miseki, H. Kusama, H. Sugihara, K. Sayama, Cs-modified WO_3 photocatalyst showing efficient solar energy conversion for O_2 production and Fe (III) ion reduction under visible light, J. Phys. Chem. Lett. 1 (2010) 1196–1200. doi:10.1021/jz100233w.

[38] S.L. Liew, Z. Zhang, T.W.G. Goh, G.S. Subramanian, H.L.D. Seng, T.S.A. Hor, H.K. Luo, D.Z. Chi, Yb-doped WO_3 photocatalysts for water oxidation with visible light, Int. J. Hydrogen Energy. 39 (2014) 4291–4298. doi:10.1016/j.ijhydene.2013.12.204.

[39] A. Cots, R. Gómez, Ytterbium modification of pristine and molybdenum-modified hematite electrodes as a strategy for efficient water splitting photoanodes, Applied Catalysis B: Environmental 219 (2017) 492-500. doi: 10.1016/j.apcatb.2017.07.067.

[40] P.-T. Hsiao, L.-C. Chen, T.-L. Li, H. Teng, Vapor treatment of nanocrystalline WO_3 photoanodes for enhanced photoelectrochemical performance in the decomposition of water, J. Mater. Chem. 21 (2011) 19402–19409. doi:10.1039/c1jm14785d.

[41] Y. Uwamino, T. Ishizuka, H. Yamatera, X-ray photoelectron spectroscopy of rare-earth compounds, J. Electron Spectros. Relat. Phenomena. 34 (1984) 67–78. doi:10.1016/0368-2048(84)80060-2.

[42] W. Li, J. Li, X. Wang, J. Ma, Q. Chen, Photoelectrochemical and physical properties of WO_3 films obtained by the polymeric precursor method, Int. J. Hydrogen Energy. 35

(2010) 13137–13145. doi:10.1016/j.ijhydene.2010.09.011.

[43] Q. Yu, X. Meng, L. Shi, G. Liu, P. Li, J. Ye, Hematite homojunctions without foreign element doping for efficient and stable overall water splitting, RSC Adv. 6 (2016) 62263–62269. doi:10.1039/C6RA13060G.

[44] M. Kosmulski, Isoelectric points and points of zero charge of metal (hydr)oxides: 50 years after Parks' review, Adv. Colloid Interface Sci. 238 (2016) 1–61. doi:10.1016/j.cis.2016.10.005.

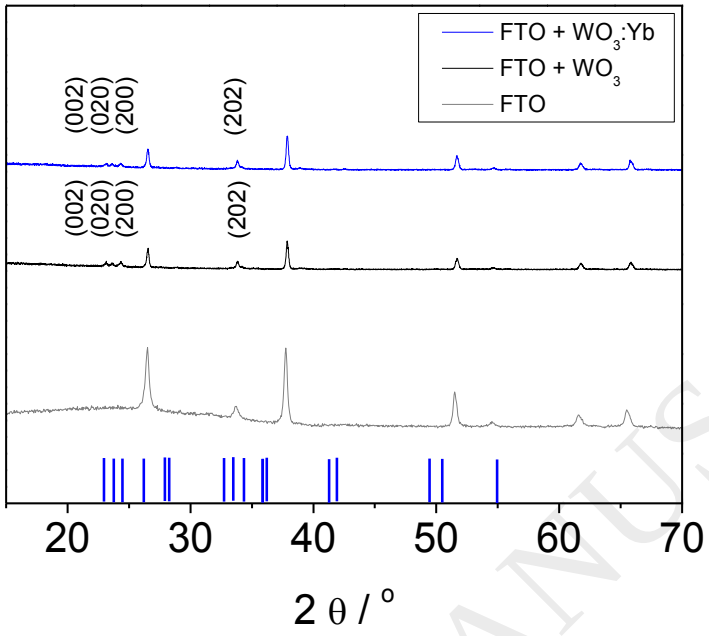

Figure 1. XRD patterns for the samples of WO_3 and WO_3:Yb 0.2 at. %.

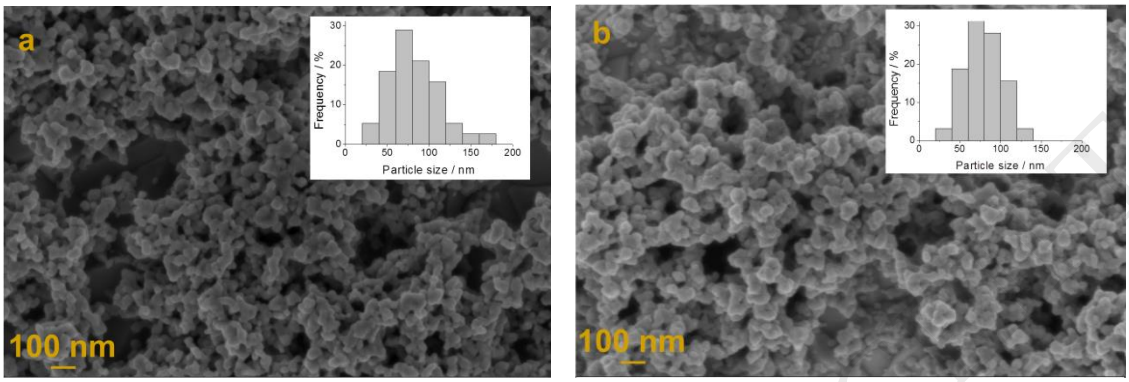

Figure 2. Scanning electron micrographs for the samples of (a) WO_3 and (b) WO_3:Yb 0.2 at%.

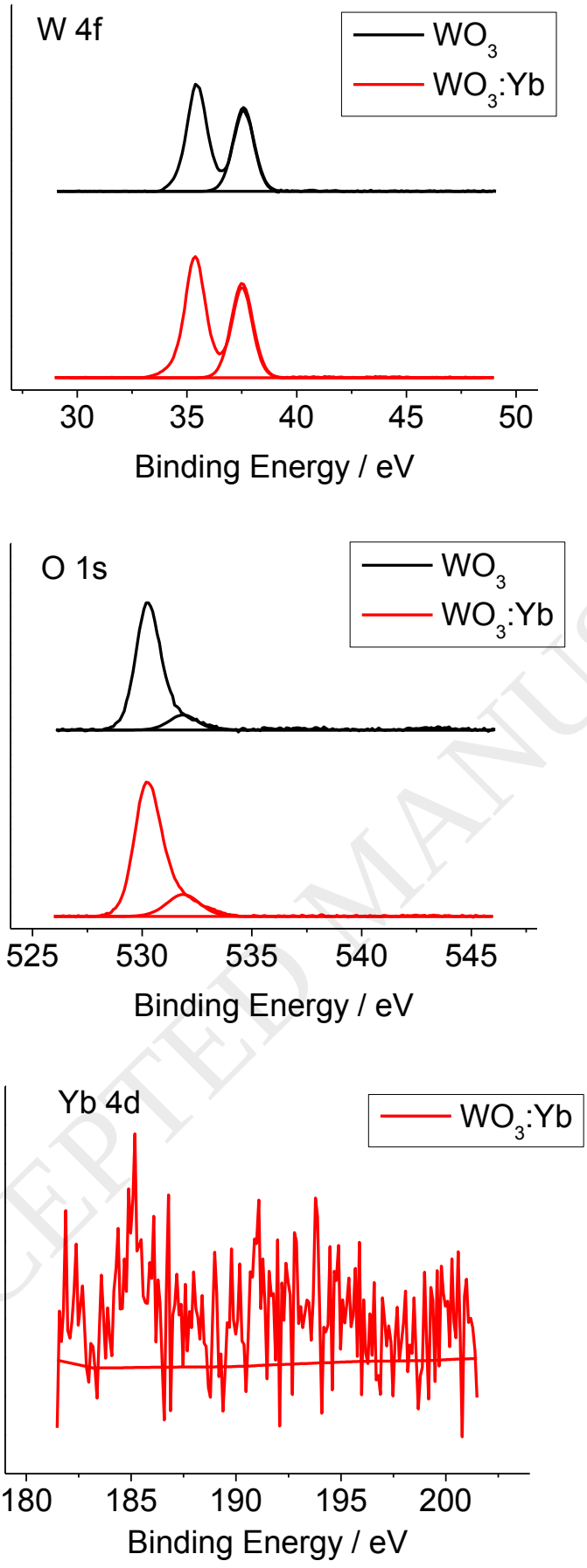

Fig. 3. XPS spectra for the samples of WO_3 and WO_3:Yb 0.2 at%.

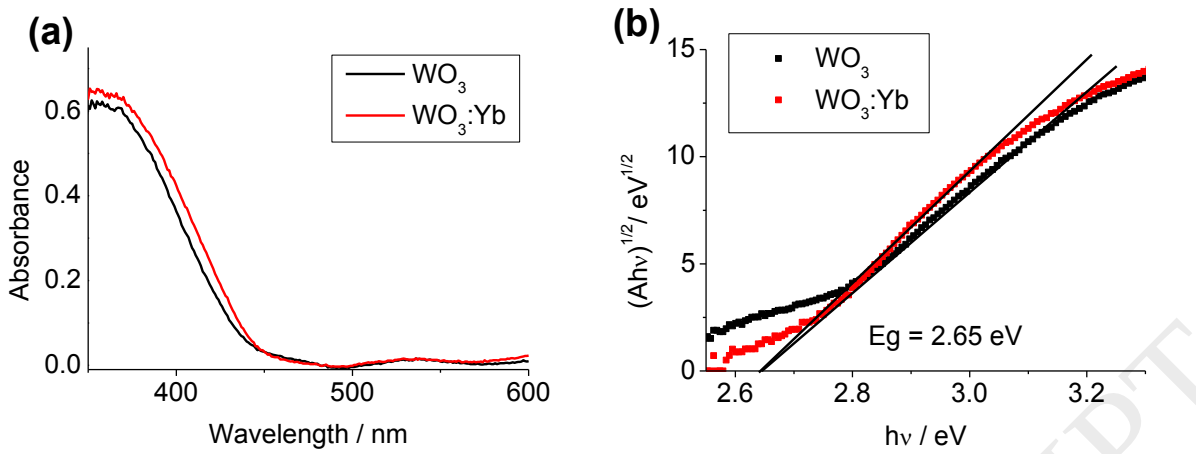

Fig. 4. (a) Optical absorbance of the samples of WO_3 and WO_3:Yb 0.2 at.%, (b) Determination of the bandgap from an $(Ahv)^{1/2}$ versus *hv* plot for WO_3 and WO_3:Yb 0.2 at% samples.

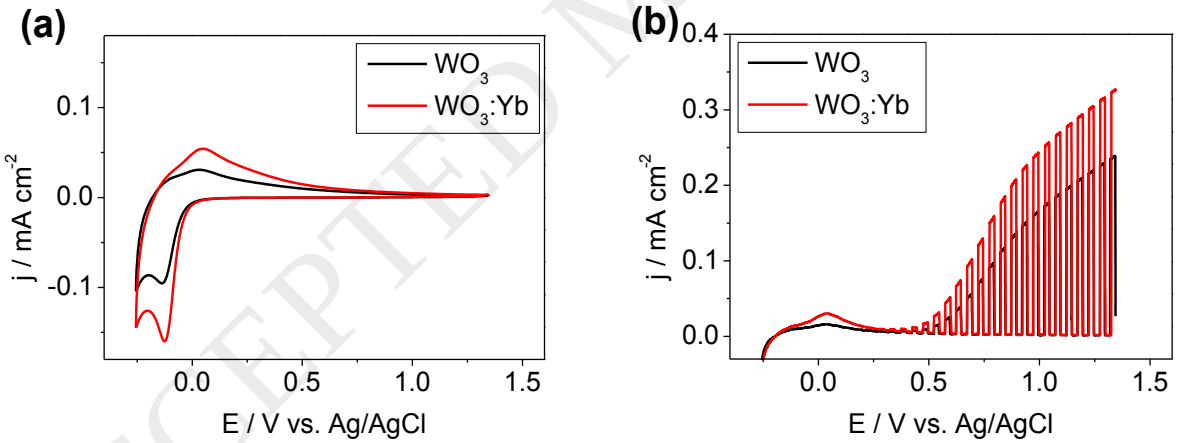

Fig. 5. (a) Cyclic voltammograms for WO_3 and WO_3:Yb 0.2 at% samples in the dark in 0.1 M $HClO_4$. Scan rate: 20 mV s^{-1}. (b) Linear scan voltammograms for the same samples under chopped illumination in 0.1 M $HClO_4$. Scan rate: 5 mV s^{-1}.

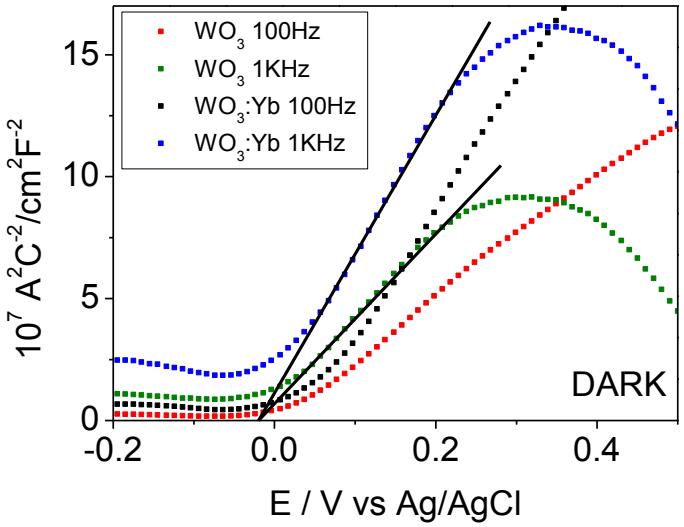

Fig. 6. Mott-Schottky plots (at two different frequencies) for WO_3 and WO_3:Yb 0.2 at% samples in 0.1 M $HClO_4$ in the dark.

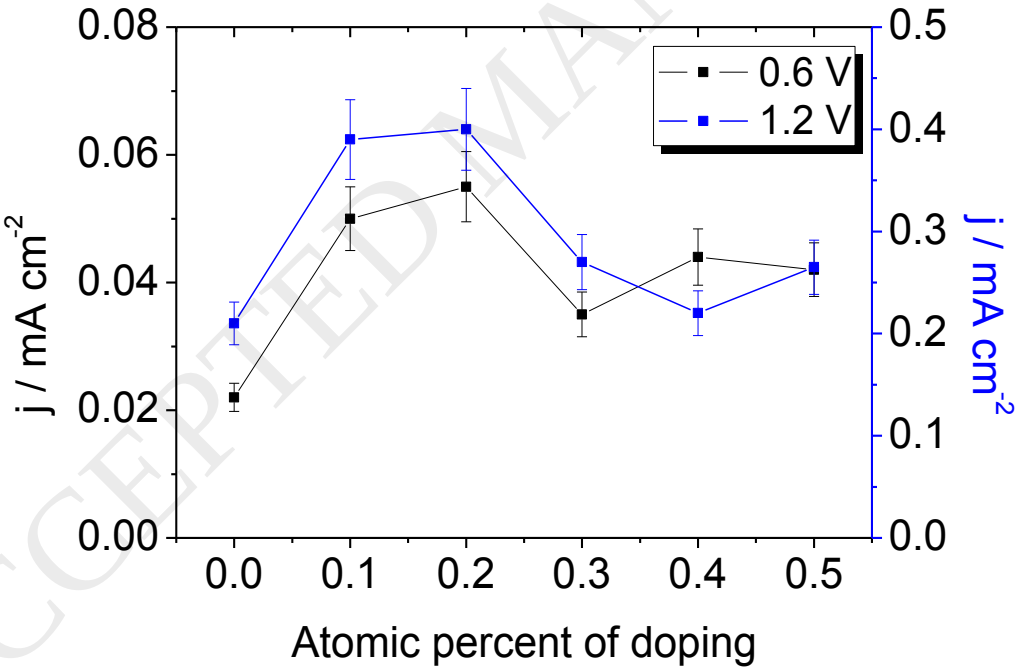

Fig. 7. Dependence of the photocurrent density on atomic percent of Yb in the WO_3 electrodes.

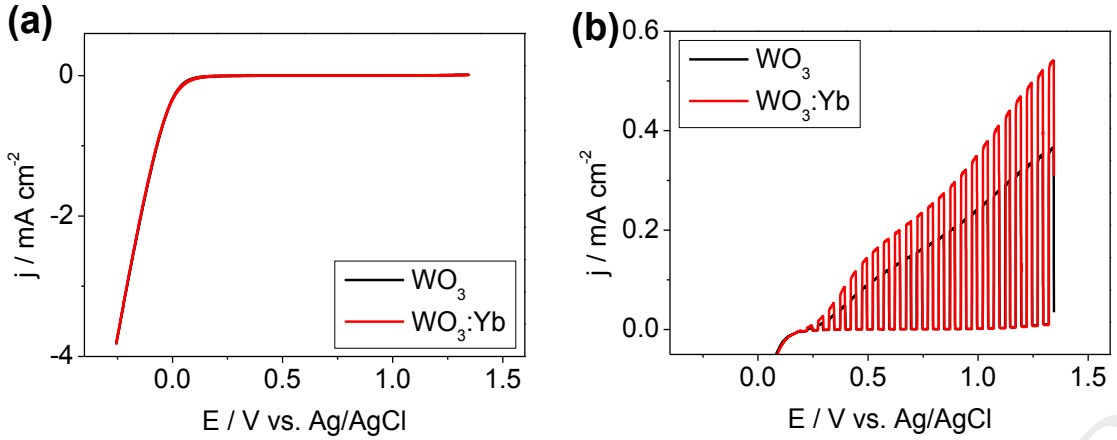

Fig. 8. (a) Cyclic voltammograms for WO_3 and WO_3:Yb 0.2 at% samples in the dark in 0.1 M $HClO_4$ and H_2O_2. Scan rate: 20 mV s^{-1}. (b) Linear scan voltammograms for the samples of WO_3 and WO_3:Yb 0.2 at. % in 0.1 M $HClO_4$ and H_2O_2. Scan rate: 5 mV s^{-1}.

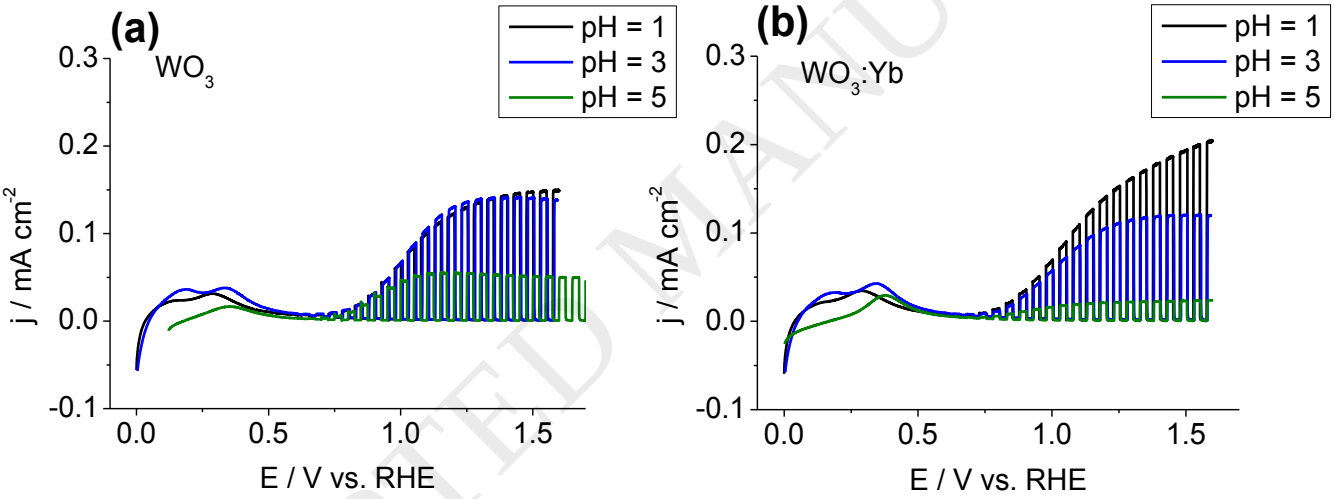

Fig. 9. Linear scan voltammograms under chopped illumination for (a) WO_3 and (b) WO_3:Yb electrodes in contact with solutions of different pH (1, 3 and 5). Scan rate: 5 mV s^{-1}.